EDGE ARTICLE

Check for updates

All publication charges for this article have been paid for by the Royal Society of Chemistry

Boosting type-I ROS production of molecular photosensitizers using bridge-assisted superexchange coupling†

Lei Chen,‡ Shirong Yan,‡ Wu-Jie Guo, Lu Qiao, Xinyue Zhan, Bin Liu [ID] * and Hui-Qing Peng [ID] *

Bridge-assisted superexchange coupling capable of long-range electron transfer proves to be effective for charge separation. However, the exploitation of this photochemical process in engineering reactive oxygen species (ROS) production remains unexplored. Herein, piperazine serves as a bridging unit to facilitate a cascade electron transfer from the electron donor site (CO) to the acceptor site (CN) within the **COCN** molecule, ultimately boosting the generation of superoxide radicals ($O_2^{-\bullet}$) and hydroxyl radicals ($^\bullet OH$). Experimental and theoretical studies elucidate that the long-range electron transfer is enabled by a superexchange interaction through the piperazine σ^*-bridge, which leads to an effective generation of a radical ion pair $CO^{+\bullet}BCN^{-\bullet}$. The cationic radical $CO^{+\bullet}$ can directly catalyze the oxidation of water, while the anionic radical $CN^{-\bullet}$ transfers one electron to oxygen (O_2). Additionally, **COCN** has an excited triplet state characterized by a $^3(\pi-\pi^*)$ electronic configuration, which further promotes sequential electron transfer to O_2. These reactions enable the efficient production of $^\bullet OH$ and $O_2^{-\bullet}$, respectively, thus completing a cascade electron cycling process. Based on these findings, nanoparticles of **COCN** exhibit satisfying $O_2^{-\bullet}$ and $^\bullet OH$ production performance even under hypoxic environments and demonstrate potent photodynamic activity in addition to a notably high fluorescence quantum yield of 62.8%, rendering them promising candidates for cellular imaging and ablation assessments. This study contributes to the advancement of photosensitizers proficient in selectively generating ROS, offering valuable insights into the underlying mechanisms that govern ROS production.

Introduction

Photosensitizers (PSs) that exhibit high efficiency in generating strong oxidizing reactive oxygen species (ROS) upon light irradiation play crucial roles in the fields of photodynamic therapy (PDT).[1,2] Under light irradiation, these PSs undergo a photophysical transition from the ground singlet state (S_0) to the excited singlet state (S_n), followed by activation to the excited triplet state (T_n) through intersystem crossing (ISC).[3–5] Ultimately, the triplet PSs interact with molecular oxygen (O_2) *via* electron transfer processes, leading to the generation of type-I ROS such as hydroxyl radicals ($^\bullet OH$) and superoxide radicals ($O_2^{-\bullet}$), and/or alternatively transfer energy to O_2 resulting in the production of singlet oxygen ($^1O_2$) as a type-II ROS. By harnessing these ROS, PDT has been widely recognized as

a promising clinical treatment modality, offering advantages of precise spatiotemporal control, minimal invasiveness, and non-drug resistance.[6,7] Normally, conventional PSs, comprising methylene blue and Eosin Y, are capable of simultaneously releasing type-I and type-II ROS through these two photosensitization pathways.[8] However, different ROS type exhibits distinct reactive and transient characteristics that can fulfill diverse biological demands.[9,10] For this reason, the development of PSs possessing selective ROS-generating properties will offer significant advantages in optimizing ROS-mediated biological applications. Concurrently, it is believed that the ability to selectively produce specific ROS types is highly beneficial to simplifying the elucidation of underlying biological effects associated with ROS.

Recently, PSs with efficient type-I ROS generation ability (type-I PSs) have attracted increasing attention due to its low dependence on O_2, thereby overcoming the diminished therapeutic effect in tumor hypoxic microenvironments.[11–15] Moreover, $O_2^{-\bullet}$, a highly cytotoxic ROS generated through the type-I mechanism, can react with proteins, DNA, and lipids, leading to irreversible cellular damage.[16,17] And $^\bullet OH$, which can be generated through the cascade bioreaction of $O_2^{-\bullet}$ or direct oxidation of water, is considered the most reactive species due to its

State Key Laboratory of Chemical Resource Engineering, Beijing Advanced Innovation Center for Soft Matter Science and Engineering, Beijing University of Chemical Technology, Beijing 100029, China. E-mail: binliu@buct.edu.cn; hqpeng@mail.buct. edu.cn

‡ These authors contributed equally to this work.

extremely high chemical reactivity towards nearly all biological molecules.[18] The predominant strategy for facilitating charge separation by enhancing donor–acceptor interactions within a molecule has laid a solid foundation for the development of type-I PSs.[19,20] By introducing light-induced intermolecular electron transfer between PSs and additional electron donors/acceptors can further boost the electron transfer pathway of PSs, which is able to overcome the rapid recombination of the photogenerated charges during their redox reactions.[21,22] These previous studies have shown the viability of preparing type-I PSs using an electron transfer cascade strategy. Nevertheless, systems involving multiple components may be susceptible to phase separation and component leakage, potentially undermining the stability and efficacy of the PSs and thereby complicating their practical applications.

In the field of photochemistry, a long-range intramolecular electron transfer (>10 Å) can also occur from a specific electron donor site (D) to a well-defined acceptor site (A) through the intermediate linkage between D and A (Scheme 1a).[23,24] For instance, the wave functions of the bridge (B) structures' σ^* orbitals enable effective propagation of electronically coupled interactions between D and A fragments.[25,26] Specifically, the LUMO of the D group overlaps with the LUMO of the σ^* orbital located on the nearest bond within the bridge, promoting electron transfer to the LUMO of the A unit and further resulting in the formation of $D^{+\cdot}BA^{-\cdot}$ species. Such bridge-assisted superexchange coupling has been extensively investigated in

quantum chemistry simulations due to its significance as a fundamental charge transfer process in chemical and biological systems, *e.g.*, the primary charge separation in bacterial photosynthesis.[27] However, compared to intermolecular electron transfer, the demonstration of long-range intramolecular electron transfer by superexchange coupling for facilitating the cascade electron transfer to O_2 remains unexplored. The triplet state of O_2 consists of two unpaired electrons occupying each of the two antibonding π orbitals (π_x^* and π_y^*) at the same energy level.[28] Therefore, we hypothesized that $O_2^{-\cdot}$ could be generated by populating one of the π^* orbitals with an electron from $D^{+\cdot}BA^{-\cdot}$. Simultaneously, the resulting cationic radical ($D^{+\cdot}$) captures an electron from the surrounding water, thereby oxidizing the water to $^{\cdot}OH$. The utilization of bridge-assisted superexchange coupling is anticipated to offer a highly desirable alternative approach for boosting type-I ROS production, enabling the development of stable and efficient type-I PSs with well-defined molecular structures and selective ROS-generating abilities.

Herein, we exploit the superexchange mechanism to facilitate the separation of electron–hole pairs in PSs for augmenting $O_2^{-\cdot}$ and $^{\cdot}OH$ generation (Scheme 1). As a proof of concept, three homologous compounds **COCO**, **COCN**, and **CNCN** were rationally designed, utilizing piperazine as the bridging unit, benzophenone (CO) as the terminal D group, and 2-(diphenylmethylene)malononitrile (CN) as the A group (Scheme 1b). Both CO and CN are presumed to be capable of readily accessing T_n
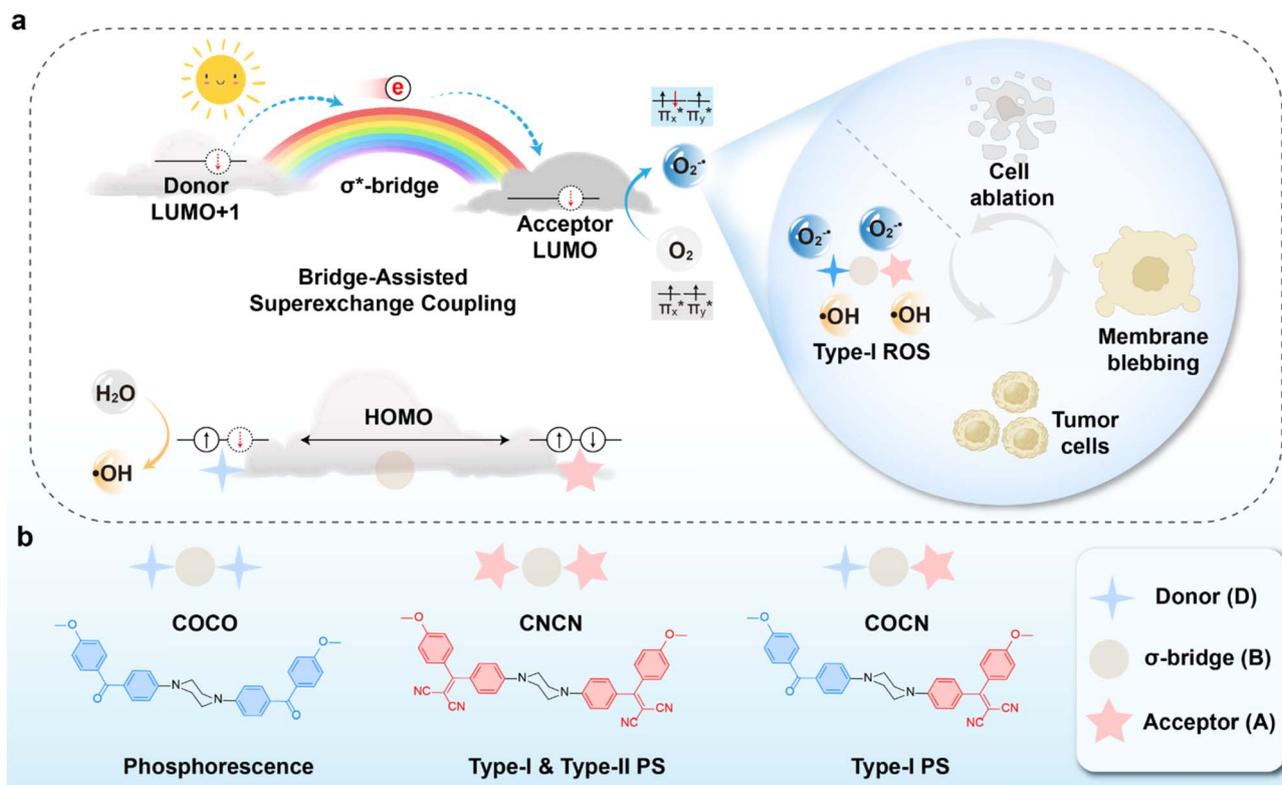
Scheme 1 (a) Schematic illustration of bridge–assisted superexchange coupling mechanism for type-I ROS generation. (b) Molecular structures of **COCO**, **CNCN**, and **COCN**.

for reacting with O_2 based on the design principle of organic phosphors.[29] Among these compounds, **COCO** exhibits persistent phosphorescence and shows minimal production of ROS, whereas **CNCN** demonstrates a remarkable ability to generate type-I and type-II ROS through two photosensitization pathways. In stark contrast, the asymmetric molecule **COCN** manifests type-I ROS-generating property, resulting in significantly enhanced production of $O_2^{-\cdot}$ and $\cdot OH$ while the generation of $^1O_2$ is negligible. Analysis of the phosphorescence lifetime and fluorescence spectra reveals that the excitation energy associated with the CO component within **COCN** has been substantially quenched by the CN group, implying an effective energy and/or electron transfer process from CO to CN. Theoretical studies verify that electron transfer occurs from the higher-energy LUMO+1 of CO to the lower-energy LUMO of CN *via* piperazine-assisted superexchange, resulting in the formation of a radical ion pair $CO^{+\cdot}BCN^{-\cdot}$. The cationic radical $CO^{+\cdot}$ catalyze the oxidation of water, resulting in the generation of $\cdot OH$. Concurrently, **COCN** has T_1 state featuring a $^3(\pi-\pi^*)$ electronic configuration, which promotes cascade electron transfer from $CN^{-\cdot}$ to O_2 for efficient generation of $O_2^{-\cdot}$. Finally, nanoparticles of **COCN** were prepared with a remarkable fluorescence quantum yield of 62.8%, while maintaining efficient $O_2^{-\cdot}$ and $\cdot OH$ production ability in aqueous solution. They were successfully employed for cellular imaging and photodynamic cancer cell ablation. To our best knowledge, this is the first demonstration of a molecular photosensitizer design using bridge-assisted superexchange coupling to facilitate cascaded electron transfer and thus enable the engineering of type-I ROS generation.

Results and discussion

The primary purpose of this study is to design selective type-I PSs based on the electron transfer cascade strategy utilizing bridge-assisted superexchange coupling. For the CO group, benzophenone is a representative organic phosphor that can efficiently transition from S_n to T_n with nearly 100% ISC yield. For the CN fragment, the incorporation of a malononitrile group with strong electron-withdrawing ability not only promotes the charge transfer (CT) effect but also substantially reinforces the intramolecular steric hindrance, which results in a nonplanar molecular conformation. Such nonplanarity can destruct $\pi-\pi$ stacking interactions and impart aggregation-induced emission (AIE) features to the compounds with CN moiety. The utilization of AIE-active PSs is expected to increase ROS generation by blocking nonradiative pathways through the restriction of molecular motions in aggregates, thereby realizing efficient fluorescence imaging-guided PDT.[30] On the other hand, as per our previous findings, piperazine has a compact small molecular structure exhibiting a rigid chair conformation. It acts as the bridging unit not only fixes the D and A units at well-defined separations through the saturated hydrocarbon linkages but also plays a pivotal role in facilitating the electron transfer process by incorporating nitrogen atoms carrying lone pairs.[31,32] Based on these reasons, the PSs in this study were designed and synthesized by involving benzophenone,

malononitrile, and piperazine as the molecular components. **COCO** was readily prepared through a nucleophilic substitution reaction between (4-fluorophenyl)-(4-methoxyphenyl)methanone and piperazine. Subsequently, **COCO** can undergo Knoevenagel condensation with malononitrile to yield **COCN** and **CNCN** (Scheme S1†). The chemical structures of **COCO**, **COCN**, and **CNCN** were thoroughly characterized by ^1H NMR, ^{13}C NMR, and high-resolution mass spectroscopies with satisfactory outcomes (Fig. S1–S9†).

The UV-vis and photoluminescence (PL) spectroscopies of **COCO**, **COCN**, and **CNCN** were systematically analyzed to gain a more comprehensive understanding of their photophysical properties. As illustrated in Fig. 1a, **COCO** in dimethyl sulfoxide (DMSO, 10 μM) exhibits maximum absorption and emission intensity at 350 nm and 500 nm, respectively. In contrast, the incorporation of the strong electron-withdrawing malononitrile group leads to a new absorption peak at 450 nm for both **COCN** and **CNCN** in DMSO (10 μM), while their emission intensity maximum peak at around 585 nm. Furthermore, the PL intensities of **COCN** and **CNCN** are observed to gradually increase in a mixture of tetrahydrofuran and water as the volume fraction of water increased, confirming their typical AIE characteristics (Fig. 1b and S10†). Nevertheless, the PL intensity of **COCO** exhibits a remarkable decrease as the fraction of the poor solvent increased due to the aggregation-caused quenching effect. Given the indispensability of accessing triplet states for ROS generation, we investigated the prompt and delayed emission spectra of **COCO**, **COCN**, and **CNCN** at the temperature of 77 K (Fig. S11†). With a delay time of 1 ms, the delayed spectra show a profile akin to their corresponding prompt spectra. This observation suggests that the emissions predominantly originate from the long-lived triplet levels, implying a high efficiency of these compounds in populating triplet excitons. The phosphorescence lifetime of **COCO** at 490 nm has been estimated to be 94.7 ms (Fig. 1c). However, the emission intensity of both **COCN** and **CNCN** is so faint that their emission lifetimes are hard to be detected. The comparative analysis of the results demonstrates that the presence of the CN group can block the relaxation of CO from the triplet state to the ground state *via* phosphorescence emission.

After confirming the excellent photostability of **COCO**, **COCN**, and **CNCN** (Fig. S12 and S13†), their overall ability to generate ROS was assessed using the commercially available 2,7-dichlorodihydrofluorescein (DCFH) as the indicator. As shown in Fig. 1d and S14,† under white light (35 mW cm^{-2}) irradiation for 300 s, the PL intensities of DCFH solution significantly increase in the presence of **COCN** or **CNCN**, reaching a remarkable 49.5- and 39.1-fold enhancement, respectively. The results reveal the effective overall ROS generation by **COCN** and **CNCN**, with **COCN** possessing superior production efficacy. By comparison, the PL intensity of DCFH exhibits minimal changes when its solution with **COCO** is exposed to white light. To specifically identify the type of ROS, 9,10-anthracenediyl-bis(methylene)-dimalonic acid (ABDA) was utilized as a probe to selectively detect $^1O_2$ (Fig. S15†). The experimental findings verify that the presence of either **COCO** or **COCN** cannot lead to significant attenuation in the ABDA

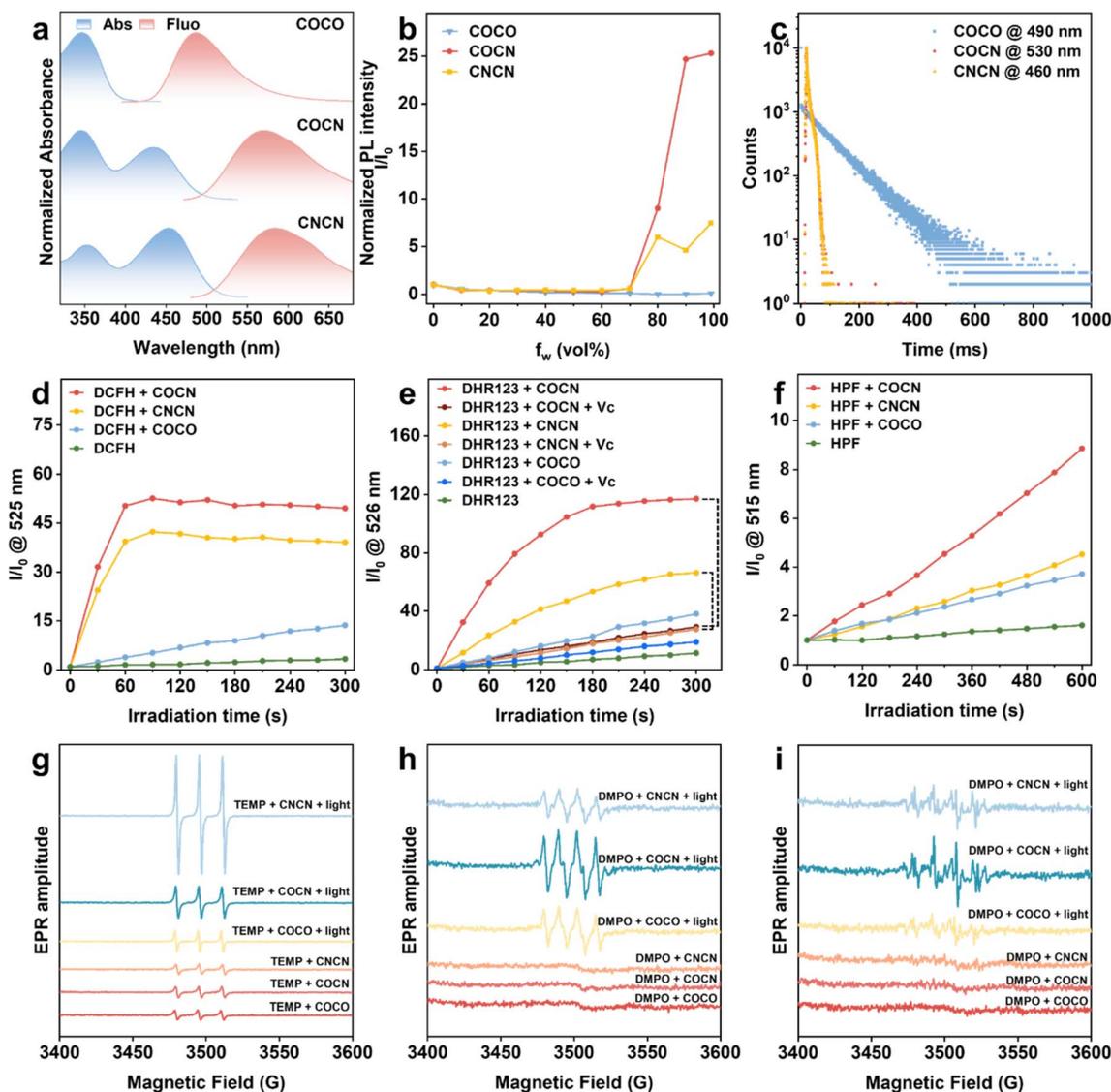Fig. 1 (a) Normalized absorption and PL spectra of **COCO**, **COCN**, and **CNCN** in DMSO. (b) Relative PL intensity (I/I_0) *versus* H_2O fraction. (c) Phosphorescent decay curves at 77 K for **COCO** (490 nm), **COCN** (530 nm), and **CNCN** (460 nm). (d) ROS generation using DCFH (1 µM) upon white light irradiation. (e) $O_2^{-\bullet}$ generation using DHR123 (10 µM) upon white light irradiation. (f) $^{\bullet}OH$ generation using HPF (10 µM) upon white light irradiation. (g) EPR spectra for $^1O_2$ detection using TEMP under irradiation. (h) EPR spectra for $O_2^{-\bullet}$ detection using DMPO in DMSO under irradiation. (i) EPR spectra for $^{\bullet}OH$ detection using DMPO in water under irradiation.

absorbance after light exposure, suggesting their limited capacity for $^1O_2$ production. Under identical conditions, an obvious reduction in absorbance is observed for the ABDA solution containing **CNCN**, indicative of type-II ROS generation by **CNCN** through the energy transfer pathway. Additionally, the generation of $O_2^{-\bullet}$ was evaluated using dihydrorhodamine 123 (DHR123) as an indicator, with vitamin C (Vc) serving as a reductant and free radical scavenger. The PL intensity of the DHR123 solution in the presence of **COCN** is apparently higher than that of observed in the presence of **CNCN** and **COCO** (Fig. 1e and S16†). Upon the addition of Vc, the fluorescence intensity of the DHR123 solution containing **COCN** is markedly reduced, with a significant 75% decrease from its maximum intensity after light irradiation for 300 s, whereas the presence

of **CNCN** in DHR123 solution results in a modest reduction, retaining 42% of the peak fluorescence intensity. Afterwards, hydroxyphenyl fluorescein (HPF) was employed as an indicator to assess the production of $^{\bullet}OH$. Upon exposure to illumination, the PL intensity of HPF solution containing **COCN** is substantially higher than that of **CNCN** and **COCO** (Fig. 1f and S17†). These findings underscore stronger $O_2^{-\bullet}$ and $^{\bullet}OH$ generation capacity of **COCN**. To further identify the ROS types, electron paramagnetic resonance (EPR) was conducted using 2,2,6,6-tetramethylpiperidine (TEMP) and 5,5-dimethyl-1-pyrroline-*N*-oxide (DMPO) as the spin-trap agents for $^1O_2$ and free radicals, respectively. Characteristic EPR signals indicative of $^1O_2$, $O_2^{-\bullet}$, and $^{\bullet}OH$ are detected in the presence of **COCO**, **COCN**, or **CNCN** under light irradiation (Fig. 1g–i). Among them, **COCN** elicits

the most intense EPR signal for both $O_2^{-\bullet}$ and $^{\bullet}OH$, while **CNCN** produces the most pronounced signal corresponding to $^{1}O_2$. Thus, we can conclude that an efficient type-I PS with free radical-generating ability has been developed.

The in-depth study of the photophysical and photochemical behaviors of **COCO**, **COCN**, and **CNCN**, as well as their different performances in the triplet states, is crucial for a fundamental understanding of the underlying mechanism associated with engineering $O_2^{-\bullet}$ and $^{\bullet}OH$ production. We conducted systematic theoretical investigations using Gaussian 09, Multiwfn, and ORCA software packages.[33–35] The transitions of the optimized states were analyzed based on the natural transition orbitals, taking into account the atomic contributions to both holes and electrons. The distribution of charge density suggests that the excitation of **COCO** arises from the local excitation of the n–π* transition, whereas the excitation of **CNCN** is attributable to the CT associated with the π–π* transition (Fig. S18†). In contrast to these symmetric structures, **COCN** displays distinct orbital occupancies for the CO and CN fragments, a disparity that can be ascribed to its asymmetrical nature at the piperazine bridge termini (Fig. 2a). In order to gain deeper insights into the distinctive properties of the σ*-bridge, the piperazine unit in **COCN** was replaced with a benzene ring, which serves as a π*-bridge and is referred to as **COPhCN** (Fig. S19†). Compared to **COCN**, the π*-bridge in **COPhCN** induces only a partial intramolecular charge transfer between the conjugated ends, making it challenging to completely separate the orbitals of the CO and CN fragments. Moreover, piperazine, acting as an electron donor, has a narrower HOMO–LUMO energy gap, thereby significantly facilitating electron transitions. Based on the isosurfaces, **COCN** can be split at the piperazine C–C σ-bond into two parts: the donor (CO) and the acceptor (CN), as shown in Fig. 2b. Considering a general electron transfer reaction (eqn (1)):

$$D^* + A \rightarrow D^{+\bullet} + A^{-\bullet} \tag{1}$$

Within the approximation of parabolic potential curves, the free energy of activation is calculated by Nelsen's four-point method (eqn (2)).

$$\Delta G^0 = [E_{D^{+\bullet}} + E_{A^{-\bullet}} - (E_D + E_A)] \tag{2}$$

The calculated free energy ΔG^0 is -2.0389 eV, and the reorganization energy λ is 2.0412 eV (Tables S1–S3†). As shown in eqn (3), the associated rate constant k_{ET} exhibits a quadratic dependence on ΔG^0 and λ.

$$k_{ET} = \nu_{eff} \exp\left[-\frac{\Delta G^0 + \lambda^2}{4\lambda kT}\right] \tag{3}$$

where ν_{eff} is the effective vibrational frequency of the electron along the reaction coordinate, k is the Boltzmann constant, and T is the temperature. This classic result, obtained by Marcus, contains a prediction: as the driving force of the reaction increases and the free energy becomes more negative, the reaction rate rises to a maximum when $-\Delta G^0 = \lambda$. Therefore,

COCN exhibits the potential for an efficient electron transfer process. However, the distance between D and A redox centers is estimated to be 10.4989 Å, which represents a relatively large D–A separation that hinders efficient electron transfer. To elucidate the long-range intramolecular electron transfer from CO to CN, the orbital distribution of piperazine was independently analyzed (Fig. 2c). The result reveals that piperazine possesses a higher energy level relative to **COCN** in both the LUMO and LUMO+1 states, enabling it to function as a bridge for efficient electron transfer. The heat map of interfragment charge transfer (IFCT) for **COCN** reveals that, following light absorption and subsequent excitation, the CN fragment captures a net total of 0.8086 electrons from the CO fragment (Fig. 2d). This pattern emphasizes the role of CO as the D fragment and CN as the A fragment, in accordance with electron transfer theory. To further validate the bridging function of piperazine, ROS generation was measured in the mixture of **CNCN** and **COCO** solution, in which CO and CN fragments are not directly connected *via* piperazine. Under identical conditions, the PL intensity enhancement of the DCFH solution containing **COCN** is 2.4-fold higher than that of the DCFH solution containing the mixture, which indicates that the enhanced type-I ROS generation of **COCN** can be attributed to its intramolecular electron transfer promoted by the piperazine bridging unit (Fig. 2e and S14†). With the aim of evaluating the electron transfer capability of **COCN**, the electrochemical experiments were carried out to elucidate its redox properties based on the energy band theory.[36] Specifically, the valence band (VB) potential of **COCN** was determined through the X-ray photoelectron spectroscopy (XPS) valence band spectrum. As presented in Fig. 2f, the maximum energy at the valence band edge was identified as 3.08 eV, which corresponds to a VB potential of 2.84 V *versus* the normal hydrogen electrode (NHE) (see ESI† for XPS analysis). Furthermore, Mott–Schottky plots were performed to assess the flat-band potential of **COCN** (Fig. 2g). The measured flat-band potential is -0.72 V *versus* NHE, which is approximately equivalent to the conduction band (CB) potential of **COCN**. Collectively, these findings indicate that the VB potential of **COCN** is more positive than the potential of $E_{OH^-/^{\bullet}OH}$ (1.99 V), and the CB potential of **COCN** is less negative than the potential of $E_{O_2^{-\bullet}/O_2}$ (-0.33 V) (Fig. 2h). These results strongly support that **COCN** is capable of photooxidizing water to $^{\bullet}OH$ and photo-reducing O_2 to $O_2^{-\bullet}$. In brief, upon photoirradiation, CO is locally excited to a higher energy state CO*. This excitation is promptly followed by an electron transfer through the piperazine bridge to the electron-deficient CN, yielding a free radical pair $CO^{+\bullet}BCN^{-\bullet}$. The subsequent interaction of $CN^{-\bullet}$ with O_2 finally leads to the production of $O_2^{-\bullet}$ (eqn (4))

$$A^{-\bullet} + O_2 \rightarrow A + O_2^{-\bullet} \tag{4}$$
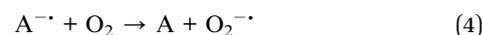
The formed cationic radical ($CO^{+\bullet}$) capture electrons from ambient water, oxidizing the water to $^{\bullet}OH$ (eqn (5)).

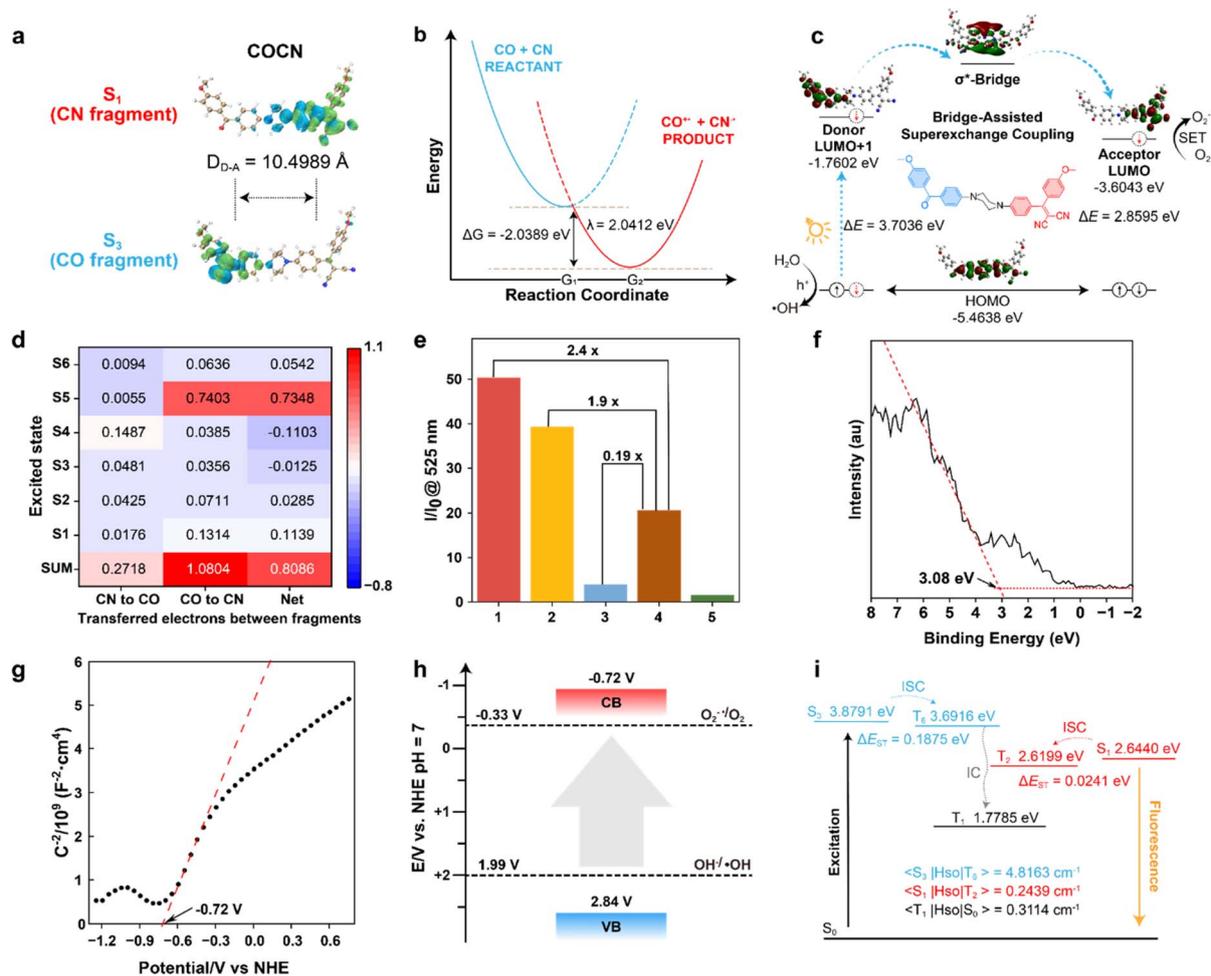$$D^{+\bullet} + OH^- \rightarrow D + {}^{\bullet}OH \tag{5}$$

Fig. 2 (a) Hole (blue)−electron (green) regions and distance of the D−A redox center (D_{D-A}) of COCN at excited states. (b) Computation scheme for Marcus parameters. (c) The HOMO, LUMO, and LUMO+1 distribution of COCN and the proposed mechanism for electron transfer *via* bridge-assisted superexchange coupling. (d) Heat map of IFCT for COCN at excited states. (e) Enhancement of fluorescence intensity of DCFH at 525 nm after 60 s white light irradiation in absence or presence of PSs ((1) COCN + DCFH, (2) CNCN + DCFH, (3) COCO + DCFH, (4) COCO + CNCN + DCFH, and (5) DCFH). (f) XPS valence band spectrum of COCN. (g) Mott−Schottky plot of COCN at 2000 Hz, measured in the dark using a carbon paper working electrode, Hg/Hg₂Cl₂ reference electrode, platinum wire counter electrode, and 1.0 M Na₂SO₄ as the supporting electrolyte. (h) Energy level diagram of COCN. (i) Energy level diagram of singlet and triplet states for COCN (CO and CN fragments) with corresponding SOC values.

Eventually, COCN returns to its ground state, enabling the completion of an electron cycling process. These findings support the adoption of a superexchange coupling mechanism for participating in the electron transfer cascade, thereby facilitating the type-I ROS generation.

To further disclose the underlying processes for $O_2^{-\bullet}$ production, a more comprehensive theoretical investigation was carried out. The electronic conformational information of COCN is provided in Tables S4–S6.† In COCN, the S_1 excited states are dominated by the $^1(\pi-\pi^*)$ transitions of CN fragment (69.5%). Concurrently, its S_3 states are mainly defined by the $^3(n-\pi^*)$ transitions of CO (65.2%). According to the EI-Sayed rule, the lowest-energy state proximal to S_1 is T_2 (with an energy gap $\Delta E_{S1-T2} = 0.0241$ eV), and the nearest $^3(\pi-\pi^*)$ to S_3 is T_6 (with a gap $\Delta E_{S3-T6} = 0.1875$ eV). These minimal energy gaps are conductive to high ISC efficiency (Fig. 2f). When contrasted

with COCO (Table S7†), it is evident that the incorporation of the CN fragment in COCN significantly reduces the T_1 energy level, while T_1 characterized by a $^3(\pi-\pi^*)$ configuration exhibits a slow decay rate owing to the forbidden spin-flip transition from $^3(\pi-\pi^*)$ to $^1\pi_2$, thus promoting the PS → O_2 electron transfer pathway for producing $O_2^{-\bullet}$. Moreover, given that spin–orbit coupling (SOC) is a dominant driving force for ISC, the SOC values of COCN for S_1 to T_2 and S_3 to T_6 are calculated to be 0.2439 cm^{-1} and 4.8163 cm^{-1}, respectively. In comparison to the photosensitizer CNCN, the inclusion of benzophenone carrying a lone pair of electrons in COCN greatly increases the likelihood of ISC (Table S8†), which ensures its high efficacy in generating ROS.

Recent studies have illustrated the benefits of type-I PSs, highlighting their capacity to maintain outstanding ROS generation performance under hypoxic microenvironments.

Leveraging this advantage, we have preliminary validated the crucial potential of **COCN** for PDT. To enhance the compatibility of our PSs for biological applications, an amphiphilic copolymer, Pluronic F127, was utilized to encapsulate **COCN** or **CNCN** for preparing water-dispersible nanoparticles (**COCN NPs** and **CNCN NPs**, respectively). Their fundamental photophysical property assessments were conducted (Fig. 3 and Table S9†). Compared to the molecular counterparts in DMSO, the absorption and emission spectra of **COCN NPs** and **CNCN NPs** have negligible changes in aqueous solution (Fig. 3a). Remarkably, the fluorescence quantum yields (QY) of **COCN NPs** and **CNCN NPs** in aqueous media are measured at 62.8% and 22.53%, respectively. These values significant surpass those of the corresponding molecules in DMSO, corroborating the distinct AIE characteristics of **COCN** and **CNCN**. Dynamic light scattering (DLS) analysis discloses that **COCN NPs** and **CNCN NPs** are well-dispersed in water with average hydrodynamic diameters of 148.7 nm and 143.7 nm, respectively (Fig. 3b). Furthermore, transmission electron microscopy (TEM) images reveal uniform spherical morphology of these **NPs**, exhibiting sizes similar to those measured using DLS. Due to the demonstrated capabilities of **COCN** and **CNCN** for ROS generation, their corresponding nanoparticles were selected for further investigation. The presence of **COCN NPs** or **CNCN NPs** under continuous light irradiation markedly intensifies the PL signals of DCFH, while a negligible increase in PL intensity is observed DCFH alone, unequivocally confirming their exceptional ROS production capabilities (Fig. S20†). To simulate the biological environment, a specific redox indicator, dihydroethidium (DHE), was combined with RNA and applied to verify the generation of $O_2^{-\cdot}$. By comparison, the PL intensity of the DHE solution containing **COCN NPs** exhibited a substantially greater enhancement under white light irradiation than the solution with **CNCN NPs** (Fig. 3c and S21†). Then, HPF as a hydroxyl radical scavenger was used to detect $\cdot$OH. The PL intensity of the HPF solution increases by a remarkable 32.2-fold in the presence of **COCN NPs**, while **CNCN NPs** enhance it by 17.1-fold after irradiation for 600 s (Fig. 3d and S22†). This provides convincing evidence that **COCN NPs** possess exceptional capacity to generate $O_2^{-\cdot}$ and $\cdot$OH for potential applications.

The high QYs of **COCN NPs** and **CNCN NPs** coupled with their robust ROS production highlight their potential for use in imaging-guided PDT. Prior to imaging, the cytotoxicity of these **NPs** toward 4T1 cancer cells were assessed using the CCK-8 assay. The 4T1 cell lines were purchased from the Cell Resource Center, Peking Union Medical College. The cell viability remains over 85% even after incubation with a 16 μM concentration of **NPs** for 24 h under dark conditions, indicative of outstanding biocompatibility and minimal dark toxicity of **COCN NPs** and **CNCN NPs** (Fig. S23†). On this basis, a concentration of 5 μM was chosen for subsequent cellular imaging studies. Live cell imaging experiments were performed on 4T1 cells incubated with the **NPs**, with evaluation via confocal laser scanning microscopy (CLSM). As shown in Fig. S24,† the fluorescence intensity within the 4T1 cells enhances over time, peaking at 4 h after **NPs** incubation, implying rapid cellular uptake of the **NPs** within this timeframe. Notably, cells treated with **COCN NPs** display the most intense fluorescence, which is consistent with their high fluorescence QY. In light of the significance of organelle-targeting specificity, co-localization experiments were performed (Fig. 4). 4T1 cells were treated with **COCN NPs**, followed by incubation with commercially available organelle-specific trackers. A significant overlap between the red signal from **COCN NPs** and the green fluorescence of the Lyso-Tracker Green is observed with a Pearson's
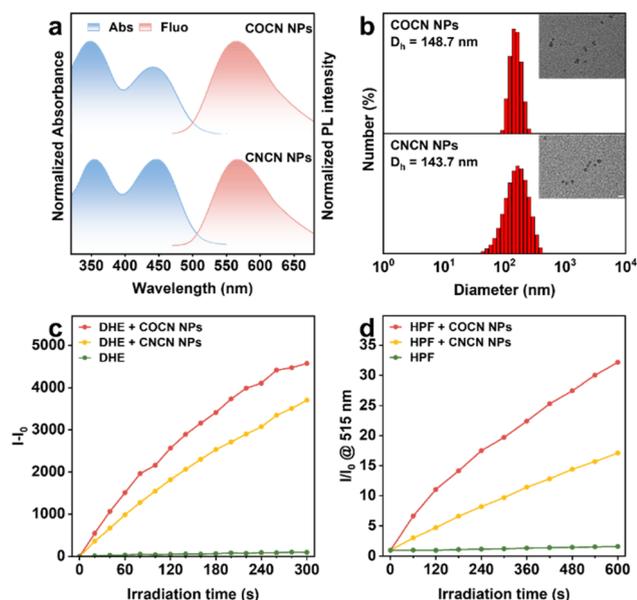

Fig. 3 (a) Normalized absorption and PL spectra of **COCN NPs** and **CNCN NPs** in water. (b) Size distribution of **COCN NPs** and **CNCN NPs**. Inset: TEM image. Scale bar: 200 nm. (c) Plots of ($I - I_0$) of DHE (40 μM) at 580 nm upon white light irradiation. (d) $\cdot$OH generation of **COCN NPs** and **CNCN NPs** (5 μM) upon white light irradiation using HPF (10 μM) as an indicator.
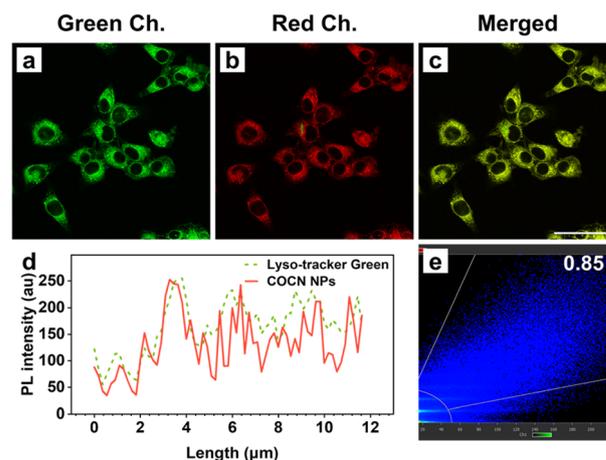

Fig. 4 Confocal fluorescence images of 4T1 cells (a–c) stained with **COCN NPs** (5 μM) and Lyso-Tracker Green (50 nM). (d) Intensity profile of ROIs between **COCN NPs** (red line) and Lyso-Tracker Green (green line). (e) Fluorescence intensity correlation plot for **COCN NPs** and Lyso-Tracker Green. Scale bar: 50 μm.

correlation coefficient as high as 0.85. This indicates a predominant accumulation of **COCN NPs** within the lysosomes.

Motivated by the efficient $O_2^{-\bullet}$ and $^{\bullet}OH$ generation and outstanding cellular imaging capabilities, the PDT performance of **COCN NPs** was studied under both normoxic and hypoxic conditions. Intracellular ROS generated by **COCN NPs** was detected using the general probe DCFH. Fig. 5a and b reveal that, following light irradiation, cells treated with **COCN NPs**

exhibit bright green fluorescence, confirming the effective ROS generation. Satisfyingly, even in hypoxic conditions, notable green fluorescence is retaining 92% intensity compared to that observed under normoxic conditions, indicating that the efficacy of **COCN NPs** is not obviously diminished hypoxia. To specifically identify the type of the intracellular ROS, the $O_2^{-\bullet}$ indicator DHE and $^{\bullet}OH$ indicator HPF were utilized. As anticipated, remarkable red and green fluorescence is observed in cells after exposure to light, both under normoxic and hypoxic
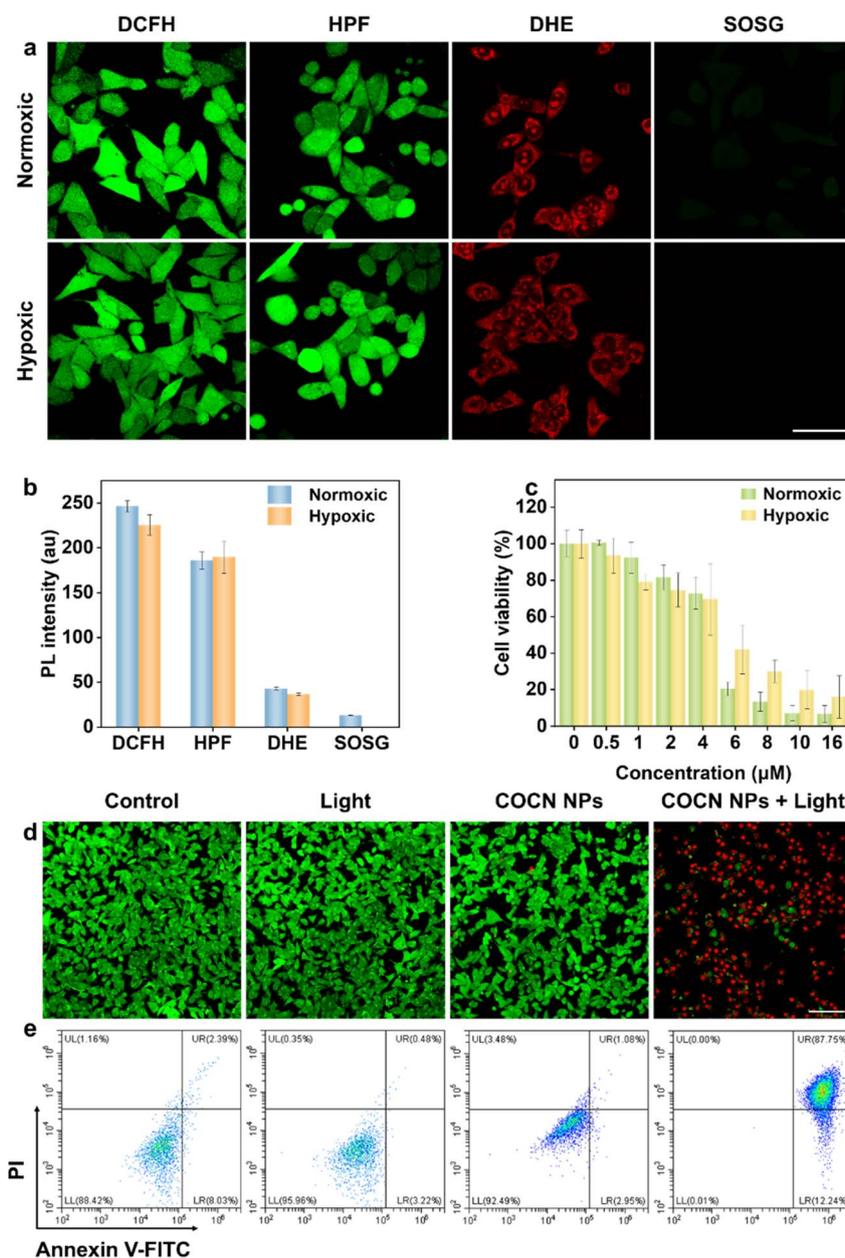

Fig. 5 (a) ROS imaging and fluorescence intensity of 4T1 cells pretreated with **COCN NPs** (5 μM) and irradiated with white light (35 mW cm^{-2}) under normoxic (21% O_2) and hypoxic (2% O_2) conditions. Scale bar: 50 μm. (b) Quantification analysis of panel (a). Data are mean ± SD ($n = 3$). (c) Viability of 4T1 cells subjected to various amounts of **COCN NPs** under normoxic and hypoxic conditions. Data are mean ± SD ($n = 3$). (d) Fluorescence images of 4T1 cells treated with **COCN NPs** (8 μM) and irradiated with white light (35 mW cm^{-2}) under normoxic conditions. The live cells were stained with Calcein-AM, and the dead cells were stained with PI. Scale bar: 100 μm. (e) Apoptosis/necrosis analysis by flow cytometry using Annexin V-FITC and PI under normoxic conditions.

conditions, which illustrates the potential ability of **COCN NPs** to yield $O_2^-\cdot$ and $\cdot OH$ even under the hypoxic microenvironment of tumor cells. Conversely, the detection of intracellular $^1O_2$ generation using the singlet oxygen sensor green (SOSG) yields starkly different results from those of DHE. Minimal green fluorescence is observed in cells under hypoxic conditions, suggesting that the predominant cytotoxic mechanism of **COCN NPs** after light exposure is through $O_2^-\cdot$ and $\cdot OH$ rather than $^1O_2$. Thereafter, the PDT effects of **COCN NPs** toward 4T1 cells under both normoxic and hypoxic conditions were evaluated using the standard CCK-8 assay. After exposure to white light for 15 min, a pronounced decline in cell viability was observed at concentrations of **COCN NPs** exceeding 4 μM in normoxic environments. Notably, similar outcomes were obtained even under hypoxic conditions. The reduction in O_2 concentration has little impact on the cytotoxicity of **COCN NPs**, further highlighting their excellent PDT efficacy regardless of O_2 levels (Fig. 5c). Further, live/dead cell staining assays with Calcein-AM (to indicate live cells with green fluorescence) and propidium iodide (PI, to indicate dead cells with red fluorescence) were performed to provide a clear visualization of the PDT efficacy. As shown in Fig. 5d and S25,† strong green fluorescence signals are detected in the three control groups, in stark contrast to the experimental group treated with **COCN NPs** and light irradiation, which exhibits predominantly red fluorescence, validating considerable cell mortality. To further elucidate the cancer-killing efficiency of **COCN NPs** at the cellular level, apoptosis/necrosis analysis was conducted employing flow cytometry with Annexin V-FITC and PI staining under normoxic conditions (Fig. 5e). It turns out that **COCN NPs** induce early apoptosis in 12.24% of cells and late apoptosis in 87.75% when exposed to white light. In contrast, either **COCN NPs** or white light irradiation alone doesn't inhibit cell growth. Collectively, these findings robustly support that **COCN NPs** possess potent therapeutic potential for cancer treatment.

Conclusions

In conclusion, we have reported the first demonstration of bridge-assisted superexchange coupling to facilitate an electron transfer cascade for engineering $O_2^-\cdot$ and $\cdot OH$ generation. By comparison, the asymmetric molecule **COCN** possesses the ability to produce $O_2^-\cdot$ and $\cdot OH$, which is remarkably distinct from **COCO** with phosphorescence property and **CNCN** that generate both type-I and type-II ROS. Experimental and theoretical studies reveal that the amplified generation of free radicals from **COCN** is achieved by a long-range electron transfer, where the CO fragment donates one electron to the CN fragment through the piperazine σ^*-bridge *via* superexchange coupling. Importantly, nanoparticles of **COCN** not only maintain their potent $O_2^-\cdot$ and $\cdot OH$ production capability but also exhibit a remarkable fluorescence high quantum yield of 62.8%. *In vitro* investigations confirm that **COCN NPs** can efficiently generate $O_2^-\cdot$ and $\cdot OH$ in cancer cells, regardless of the intracellular O_2 level and thereby showcase excellent phototoxicity against cancer cells. Compared to intermolecular electron transfer, the utilization of bridge-assisted superexchange

coupling to achieve long-range intramolecular electron transfer in a single molecule potentially offers the advantages of establishing a more explicit structure–activity relationship and enhancing stability. This approach is expected to be beneficial for the future advancement of PSs with selective ROS-generating properties for optimizing their biological effects and simplifying the underlying mechanisms. However, our photosensitizer's short emission wavelength limits its application in *in vivo* imaging and PDT. The development of red/NIR light-emitting PSs based on such an electron transfer cascade strategy for *in vivo* studies is currently ongoing in our laboratory.

Data availability

Experimental procedures and the data supporting this article have been included as part of the ESI.†

Author contributions

L. C. synthesized materials, performed all measurements, and wrote the manuscript. S. Y. designed and directed the investigations and composed the manuscript. W.-J. G., L. Q., and X. Z. revised the manuscript. B. L. and H.-Q. P. provided intellectual input and revised the manuscript. All the authors were involved the analysis of results and discussions of the project.

Conflicts of interest

There are no conflicts to declare.

Acknowledgements

Notes and references

1 X. Li, J. F. Lovell, J. Yoon and X. Chen, *Nat. Rev. Clin. Oncol.*, 2020, **17**, 657–674.

2 D. E. J. G. J. Dolmans, D. Fukumura and R. K. Jain, *Nat. Rev. Cancer*, 2003, **3**, 380–387.

3 Z. Li, Z. Zhou, Y. Wang, J. Wang, L. Zhou, H.-B. Cheng and J. Yoon, *Coord. Chem. Rev.*, 2023, **493**, 215324.

4 J. Li, Z. Zhuang, Z. Zhao and B. Z. Tang, *View*, 2022, **3**, 20200121.

5 X. Zhao, J. Liu, J. Fan, H. Chao and X. Peng, *Chem. Soc. Rev.*, 2021, **50**, 4185–4219.

6 Q. Sun, Q. Su, Y. Gao, K. Zhou, W. Song, P. Quan, X. Yang, Z. Ge, Y. Zhang and G. He, *Aggregate*, 2023, **4**, e298.

7 S. Liu, Y. Pei, Y. Sun, Z. Wang, H. Chen, D. Zhu, M. R. Bryce, B. Z. Tang and Y. Chang, *Aggregate*, 2024, **5**, e547.

8 H. Wang, W.-G. Li, K. Zeng, Y.-J. Wu, Y. Zhang, T.-L. Xu and Y. Chen, *Angew. Chem., Int. Ed.*, 2019, **58**, 561–565.

9 X. Wu, M. Yang, J. S. Kim, R. Wang, G. Kim, J. Ha, H. Kim, Y. Cho, K. T. Nam and J. Yoon, *Angew. Chem., Int. Ed.*, 2022, **61**, e202200808.

10 D. Chen, Q. Xu, W. Wang, J. Shao, W. Huang and X. Dong, *Small*, 2021, **17**, 2006742.

11 K.-X. Teng, D. Zhang, B.-K. Liu, Z.-F. Liu, L.-Y. Niu and Q.-Z. Yang, *Angew. Chem., Int. Ed.*, 2024, **63**, e202318783.

12 K.-X. Teng, W.-K. Chen, L.-Y. Niu, W.-H. Fang, G. Cui and Q.-Z. Yang, *Angew. Chem., Int. Ed.*, 2021, **60**, 19912–19920.

13 W. Chen, Z. Wang, M. Tian, G. Hong, Y. Wu, M. Sui, M. Chen, J. An, F. Song and X. Peng, *J. Am. Chem. Soc.*, 2023, **145**, 8130–8140.

14 M. Li, J. Xia, R. Tian, J. Wang, J. Fan, J. Du, S. Long, X. Song, J. W. Foley and X. Peng, *J. Am. Chem. Soc.*, 2018, **140**, 14851–14859.

15 R. Lin, J. Liu, W. Xu, Z. Liu, X. He, C. Zheng, M. Kang, X. Li, Z. Zhang, H.-T. Feng, J. W. Y. Lam, D. Wang, M. Chen and B. Z. Tang, *Adv. Mater.*, 2023, **35**, 2303212.

16 J. An, S. Tang, G. Hong, W. Chen, M. Chen, J. Song, Z. Li, X. Peng, F. Song and W.-H. Zheng, *Nat. Commun.*, 2022, **13**, 2225.

17 K. Zhang, Z. Yu, X. Meng, W. Zhao, Z. Shi, Z. Yang, H. Dong and X. Zhang, *Adv. Sci.*, 2019, **6**, 1900530.

18 Y. Wang, Y. Li, Z. Zhang, L. Wang, D. Wang and B. Z. Tang, *Adv. Mater.*, 2021, **33**, 2103748.

19 D. Li, X. Chen, D. Wang, H. Wu, H. Wen, L. Wang, Q. Jin, D. Wang, J. Ji and B. Z. Tang, *Biomaterials*, 2022, **283**, 121476.

20 S. Ning, M. Lyu, D. Zhu, J. W. Y. Lam, Q. Huang, T. Zhang and B. Z. Tang, *ACS Nano*, 2023, **17**, 10206–10217.

21 X. Hu, Z. Fang, F. Sun, C. Zhu, M. Jia, X. Miao, L. Huang, W. Hu, Q. Fan, Z. Yang and W. Huang, *Angew. Chem., Int. Ed.*, 2024, **63**, e202401036.

22 K.-X. Teng, L.-Y. Niu and Q.-Z. Yang, *J. Am. Chem. Soc.*, 2023, **145**, 4081–4087.

23 M. Natali, S. Campagna and F. Scandola, *Chem. Soc. Rev.*, 2014, **43**, 4005–4018.

24 M. U. Winters, K. Pettersson, J. Mårtensson and B. Albinsson, *Chem.–Eur. J.*, 2005, **11**, 562–573.

25 O. S. Wenger, *Chem. Soc. Rev.*, 2011, **40**, 3538–3550.

26 C. Lambert, G. Nöll and J. Schelter, *Nat. Mater.*, 2002, **1**, 69–73.

27 M. Plato, K. Moebius, M. E. Michel-Beyerle, M. Bixon and J. Jortner, *J. Am. Chem. Soc.*, 1988, **110**, 7279–7285.

28 Y. Nosaka and A. Y. Nosaka, *Chem. Rev.*, 2017, **117**, 11302–11336.

29 W. Zhao, Z. He and B. Z. Tang, *Nat. Rev. Mater.*, 2020, **5**, 869–885.

30 Z. Zhao, H. Zhang, J. W. Y. Lam and B. Z. Tang, *Angew. Chem., Int. Ed.*, 2020, **59**, 9888–9907.

31 W. Zhu, Z. Ding, S. Guo, W.-J. Guo, S. Yan, B. Liu, H. Li, Z. Liu, B. Z. Tang and H.-Q. Peng, *Small*, 2024, 2309424.

32 T. Peng and H.-Q. Peng, *J. Mater. Chem. C*, 2023, **11**, 12894–12899.

33 Z. Liu, T. Lu and Q. Chen, *Carbon*, 2020, **165**, 461–467.

34 T. Lu and F. Chen, *J. Comput. Chem.*, 2012, **33**, 580–592.

35 T. Lu and F. Chen, *Acta Chim. Sin.*, 2011, **69**, 2393–2406.

36 P. Gai, W. Yu, H. Zhao, R. Qi, F. Li, L. Liu, F. Lv and S. Wang, *Angew. Chem., Int. Ed.*, 2020, **59**, 7224–7229.